FRONTIERS OF PHYSICS

RESEARCH ARTICLE
Volume 18 / Issue 5 / 52304 / 2023

Photonic graphene with reconfigurable geometric structures in coherent atomic ensembles

Fuqiang Niu[1,2], Hengfei Zhang[1,2], Jinpeng Yuan[1,2,†], Liantuan Xiao[1,2], Suotang Jia[1,2], Lirong Wang[1,2,‡]

1 State Key Laboratory of Quantum Optics and Quantum Optics Devices, Institute of Laser Spectroscopy, Shanxi University, Taiyuan 030006, China
2 Collaborative Innovation Center of Extreme Optics, Shanxi University, Taiyuan 030006, China
Corresponding authors. E-mail: †yjp@sxu.edu.cn, ‡wlr@sxu.edu.cn
Received February 18, 2023; accepted April 10, 2023

ABSTRACT

Photonic graphene, possesses a honeycomb-like geometric structure, provides a superior platform for simulating photonic bandgap, Dirac physics, and topological photonics. Here, the photonic graphene with reconfigurable geometric structures is demonstrated in a $5S_{1/2} - 5P_{3/2} - 5D_{5/2}$ cascade-type ^{85}Rb atomic ensembles. A strong hexagonal-coupling field, formed by the interference of three identical coupling beams, is responsible for optically inducing photonic graphene in atomic vapor. The incident weak probe beam experiences discrete diffraction, and the observed pattern at the output plane of vapor cell exhibits a clear hexagonal intensity distribution. The complete photonic graphene geometries from transversely stretched to longitudinally stretched are conveniently constructed by varying the spatial arrangement of three coupling beams, and the corresponding diffraction patterns are implemented theoretically and experimentally to map these distorted geometric structures. Moreover, the distribution of lattice sites intensity in photonic graphene is further dynamically adjusted by two-photon detuning and the coupling beams power. This work paves the way for further investigation of light transport and graphene dynamics.

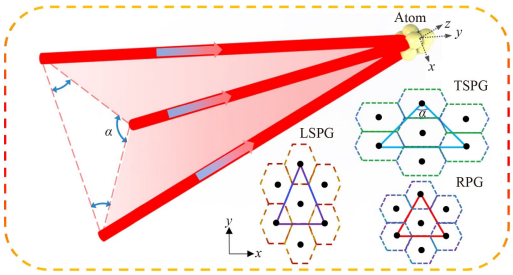

Keywords atomic ensembles, photonic graphene, geometric structures, discrete diffraction

1 Introduction

Artificial periodic structures give us the ability to achieve conventional natural structures (e.g., grating and graphene) in photonic materials [1] using artificial methods, which further promote our understanding and simulation of the basic physical rules of natural structures [2–6]. Photonic graphene, as an ongoing advanced artificial periodic structure, is an analogue of graphene in photonic simulations [7, 8] and exhibits certain specific graphene-like properties. Photonic graphene possesses the refractive index with the honeycomb profile, and makes the observation of the unusual movement of photons in connection with the physics of Dirac points possible, which are difficult to realize in natural graphene [9, 10] and finds applications in photonic devices, such as electromagnetic wave shielding [11] and valley-dependent beam manipulators [12].

Nowadays, photonic graphene is conventionally fabricated in solid materials via the femtosecond laser writing technique [13], which moves samples along the pre-calculated path using a focusing femtosecond laser [14]. This

Higher Education Press

https://doi.org/10.1007/s11467-023-1294-2

technique is widely used for the accurate fabrication of various periodic structures with specific parameters, and the generated structures are utilized in micromachining [15] and photonic devices [16]. However, the refractive index of the resulting periodic structures is usually non-tunable, thus leading to the common limitation in solid materials and preventing further investigations of photonic graphene [17]. As an alternative, the optically induced method based on electromagnetically induced transparency (EIT) which is a typical quantum coherent effect [18], has been proposed as an efficiency way to generate tunable photonic lattices in atomic medium [19–27]. Such electromagnetically induced lattices (EIL) promise the fundamental researches of lop-sided Raman–Nath diffraction [28], Bloch oscillation [29, 30], and Bragg diffraction [31], and the excellent properties of these lattices also lead to the generation of novel all-optical devices [32–34]. Specifically, photonic graphene in coherent atomic ensembles is constructed by replacing the traveling-wave coupling field with a three-beam interfering standing-wave field under EIT condition, which opens the possibility of simulating graphene dynamics in atomic medium.

As a result, the optical properties of photonic graphene in atomic medium can be efficiently tuned by systematic parameters, which promises tremendous research prospects for studying topological photonics [35, 36]. Photonic graphene has specific photonic bandgap structure, proves a novel platform for research of optical vortices in wave packets in topological defects [37]. In recent years, the photonic graphene in atomic medium has introduced more striking features into physics of edge states, resulting in the observation of edge solitons at the zigzag edge [38]. Additionally, the photonic graphene exhibits strong spatial gradients of permittivity, which leads to spin–orbit coupling and provides a correction to the paraxial beam equations [39]. Furthermore, photonic graphene implemented in an atomic vapor cell is used to study the perfect Klein transmission at normal incidence and a large decrease of the transmission with increasing incidence angle, which are in excellent agreement with the theoretical simulation based on the Dirac equation [40]. These proposed researches are all potential applications of photonic graphene, paving the way for further experimental explorations of topological photonics, while more geometric structures of photonic graphene, such as stretched photonic graphene, are usually hard to construct and have even more fascinating structural properties, which provides the possibility for the research of valley Hall effect and topological insulator in atomic medium [41, 42]. However, to the best of our knowledge, photonic graphene with stretched geometric structures in the atomic medium have not been experimentally demonstrated yet.

In this work, we achieve the photonic graphene with reconfigurable geometric structures in a three-level cascade-type ^{85}Rb atomic medium. Three identical coupling beams, propagate along the z-axis to inject into the ^{85}Rb vapor cell, interfere with each other at a small angle to induce the photonic graphene. A Gaussian probe beam traveling through the atomic vapor is modulated by the induced photonic graphene and a clear diffraction pattern with hexagonal intensity distribution is observed. The stretched geometries of photonic graphene from transverse direction to longitudinal direction are conveniently implemented by varying the spatial arrangement of three coupling beams, and the diffraction patterns of the probe beam in photonic graphene with the different geometric structures are observed experimentally. Furthermore, the dynamic tunability of lattice sites intensity in photonic graphene is further manipulated by two-photon detuning and the coupling beams power. This work paves the way for further investigation of light transport [43–45] and graphene dynamics [46, 47].

2 Experimental setup

The experimental implementation of photonic graphene with reconfigurable geometric structures is shown in Fig. 1(a), which is worked based on a three-level cascade-type ^{85}Rb atomic structure shown in Fig. 1(b). The atoms are excited from the ground state ($|5S_{1/2}, F = 2\rangle$) to an intermediate state ($|5P_{3/2}, F = 2\rangle$) using a 780 nm probe beam, and are further excited to the final state ($|5D_{5/2}, F = 1\rangle$) by a 776 nm coupling beam.

A tapered-amplified diode laser (TA pro, Toptica) operating at 776 nm, frequency shifted by a frequency shift module (FSM, a double-pass configuration based on the acoustic optical modulator), is first expanded by a beam expander (BE), and then divided by a beam splitting control system (BSCS, contains a beam-splitting module and a position control module (PCM)) into three identical beams. The diameter of the coupling beams in circular profile is ~1800 μm, which is measured in the equivalent center position of vapor cell by a charge-coupled device (CCD). These three coupling beams interfere with each other along the z-axis at a small angle θ, forming a coupling field with a hexagonal profile in the atomic vapor to induce the lattice with a honeycomb-like susceptibility distribution [38]. The 780 nm probe beam is provided by an external cavity diode laser (DL pro, Toptica), the frequency of which is also shifted by an FSM. The diameter of the probe beam in circular profile is ~300 μm, which is measured by the same method as coupling beams. The probe beam counter-propagates through the hexagonal-coupling field inside the atomic vapor. It is diffracted by photonic graphene having different geometric structures into hexagonal patterns under EIT condition and recorded by a CCD real-time. Furthermore, the pure ^{85}Rb vapor cell is 2.5 cm in diameter

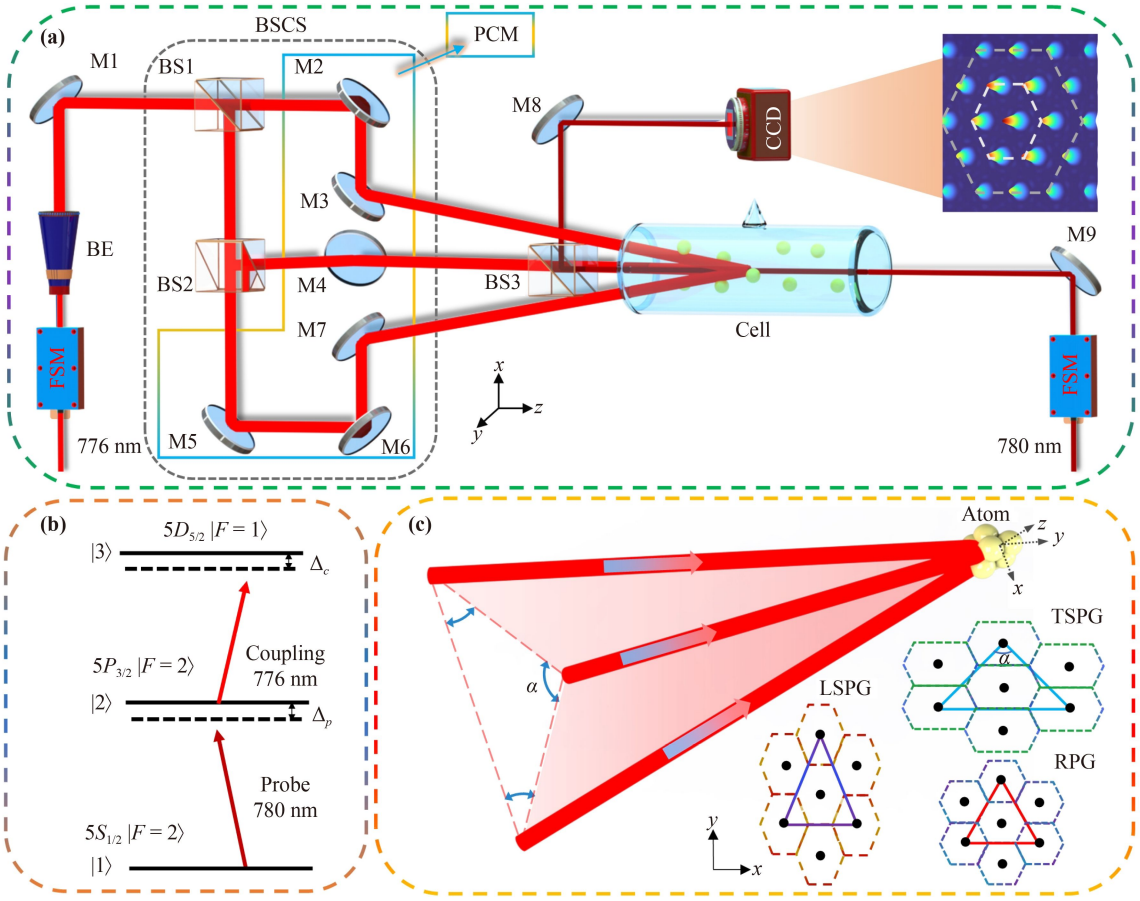

Fig. 1 **(a)** Experimental setup. FSM, frequency shift module; BE, beam expander; BSCS, beam splitting control system; PCM, position control module; M, high reflection mirror; BS, beam splitter; CCD, charge-coupled device **(b)** Relevant energy levels of the ^{85}Rb atomic system. **(c)** Schematic diagram of generating the stretched photonic graphene. TSPG, transversely stretched photonic graphene; RPG, regular photonic graphene; LSPG, longitudinally stretched photonic graphene.

and 10 cm in length, and the temperature of the atomic vapor cell is controlled at about 363 K with the atomic density of $\sim 3.11 \times 10^{12}$ cm^{-3}. The atomic ensembles form a uniform effective medium as the thermal motion of hot atoms is stronger. Different from the cold atomic system, the interaction of light takes place with atomic group in the hot atomic system instead of individual, discrete atoms.

Figure 1(c) exhibits the spatial beam geometry of three coupling beams (before entering the cell) in the x–y plane as an isosceles triangle. The vertex angle can be controlled by an PCM (consist of three groups high reflection mirrors of M2-M7) to induce the different geometries of photonic graphene with arbitrarily controllable stretched degree in atomic vapor, including regular, transversely stretched, and longitudinally stretched photonic graphene [see in the insert of Fig. 1(c)].

3 Results and discussion

The hexagonal-coupling field with different spatial configurations, formed by the interference of the three beams, is expressed as

$$\begin{aligned}\widetilde{\Omega}_c =& \Omega_c \exp(\mathrm{i}k_0\boldsymbol{b}_1\cdot\boldsymbol{r}) + \Omega_c \exp(\mathrm{i}k_0\boldsymbol{b}_2\cdot\boldsymbol{r}) \\ &+ \Omega_c \exp(\mathrm{i}k_0\boldsymbol{b}_3\cdot\boldsymbol{r}),\end{aligned} \tag{1}$$

where Ω_c represents the Rabi frequency of the coupling beams, $\boldsymbol{b}_1 = (0,1)$, $\boldsymbol{b}_2 = (\frac{3}{2}\tan\frac{\alpha}{2}, -\frac{1}{2})$, $\boldsymbol{b}_3 = (-\frac{3}{2}\tan\frac{\alpha}{2}, -\frac{1}{2})$, and α is the vertex angle, as shown in Fig. 1(c). The changes of vertex angle lead to the generation of the hexagonal-coupling fields with different spatial configurations and induce photonic graphene with different geometries. The regular photonic graphene is induced when $\alpha = 60°$. The photonic graphene stretched along the y direction when $\alpha < 60°$, which names as longitudinally stretched photonic graphene (LSPG). On the contrary, the photonic graphene stretched along the x direction when $\alpha > 60°$, which names as transversely stretched photonic graphene (TSPG). Here, the lattice constant d_y in y direction and the lattice constant d_o in other direction are defined in photonic graphene, where $d_y = \lambda_c/(2\sin\theta_y)$, $d_o = \lambda_c/(2\sin\theta_o)$, $\theta_y = \arctan\frac{1}{z}$, $\theta_o = \arctan\left\{\left[\frac{1}{4} + \left(\frac{3}{2}\tan\frac{\alpha}{2}\right)^2\right]/z\right\}$, z is the distance of atomic vapor cell and the isosceles triangle which is formed by three coupling beams,

$\theta_m (m = y, o)$ are the small angle between the coupling beams and z-axis, and λ_c is the wavelength of the coupling beam. The minimum lattice constant is about 22 μm.

The susceptibility of the three-level cascade-type atomic structure, which is associated with the dispersion and absorption of the probe field, remains invariant along the atomic cell, and can be described as [48]

$$\chi = -\frac{N|\mu_{12}|^2}{\varepsilon_0 \hbar}\left(\gamma_{21} - \mathrm{i}\Delta_p + \frac{\left|\widetilde{\Omega}_c\right|^2}{\gamma_{32} - \mathrm{i}\Delta}\right)^{-1}, \tag{2}$$

where N is the density of the atomic ensemble, which is negligible affected by the incident laser in the hot atomic system, ε_0 is the vacuum permittivity, μ_{12} is the transition dipole momentum between levels $|1\rangle$ and $|2\rangle$, $\Delta = (\Delta_p + \Delta_c)$ is two-photon detuning, Δ_p and Δ_c are the frequency detunings of the probe and coupling beams, and $\gamma_{ij} = \frac{1}{2}(\Gamma_i + \Gamma_j)$ $(i, j = 1, 2, 3)$ with Γ_i are the decay rates of the corresponding levels, which are $\Gamma_1 = 0$ (since levels $|1\rangle$ is ground state), $\Gamma_2 = 2\pi \times 6.06$ MHz, and $\Gamma_3 = 2\pi \times 0.45$ MHz.

The transmission function of a weak probe beam at the output surface of the cell $(z = L)$ can be expressed as [18]

$$T(x, y) = \exp\left(-\frac{k\chi'' L}{2} + \frac{\mathrm{i}k\chi' L}{2}\right), \tag{3}$$

where χ' and χ'' are the real and imaginary parts of the susceptibility, respectively. $k = 2\pi/\lambda_p$ is the wave vector of the probe beam, and λ_p is the wavelength of the probe beam.

It can be seen from Eq. (2) that the susceptibility can be periodically modulated by $\widetilde{\Omega}_c$. The dispersion (χ') and absorption (χ'') properties of the probe beam at the nodes and antinodes of photonic graphene are shown in Figs. 2(a) and (b), respectively. The probe field is absorbed strongly at the nodes and almost transmitted at the antinodes (see the red lines), and its dispersion is positive at the nodes but negative at the antinodes within the EIT window (see the blue lines). This leads to a substantial periodical modulation across the probe beam and can also open the possibility of a phase modulation [48] by detuning the frequencies of the probe and coupling fields away from the resonance transition. Figures 2(c) and (d) are the amplitude and phase of the transmission function $T(x, y)$ with two-photon detuning of $\Delta = 5\Gamma_2$ over four space periods. This indicates that not only does the χ'' carry the amplitude modulation and has a hexagonal intensity distribution [Fig. 2(c)], but also the χ' delivers the phase modulation and exhibits a regular graphene profile [Fig. 2(d)]. These properties lead to the generation of photonic graphene in atomic ensembles which is efficiently diffracted to the probe beam. Figures 2(e) and (f) show the simulated

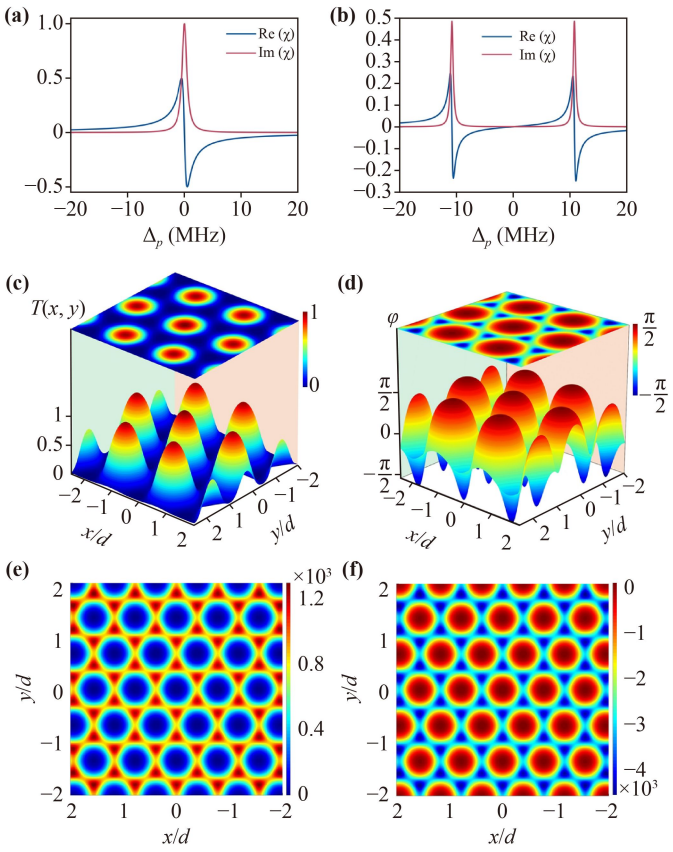

Fig. 2 Absorption and dispersion intensity at **(a)** nodes and **(b)** anti-nodes. Here, $\Delta_c = 0$. Amplitude **(c)** and phase **(d)** of the transmission function $T(x, y)$. Here, $\Delta = 5\Gamma_2$. The refractive indices of the probe beam experienced in photonic graphene with different two-photon detunings of **(e)** $\Delta = -2\Gamma_2$, **(f)** $\Delta = \Gamma_2$. Here, $\Omega_c = 2\Gamma_2$, $\Gamma_1 = 0$ and $\Gamma_3 = 0.1\Gamma_2$.

spatial refractive indices with different two-photon detunings, mainly determined by the real part of susceptibility with a negligibly small imaginary part [38]. In Fig. 2(e), the refractive index exhibits honeycomb profile with $\Delta < 0$. Its values at the honeycomb sites are big and in the hexagonal ones are small. When $\Delta > 0$, the sites with the maximum and the minimum values of refractive index are inverted with those for $\Delta < 0$, but still exhibits honeycomb-like profile as shown in Fig. 2(f) [49].

In the far-field diffraction case, the diffraction intensity can be obtained following [26]

$$I(x, y) = \left|\frac{\exp(\mathrm{i}kz)}{\mathrm{i}\lambda_i z}\exp\left[\mathrm{i}\frac{k}{2z}\left(x^2 + y^2\right)\right] \times F\left[E_p\left(x', y'\right) \times T\left(x', y'\right)\right]\right|^2, \tag{4}$$

where F represents the Fourier transform, (x, y) is the coordinate of the far-field, and (x', y') is the coordinate of the diffraction. The probe beam is the Gaussian distribution, and is expressed as [50]

$$E_p = \frac{1}{\omega_0\sqrt{1+\xi^2}} \exp\left[ikz - \frac{1-i\xi}{\omega_0^2(1+\xi^2)}r^2 - i\arctan(\xi)\right], \tag{5}$$

where ω_0 is the beam waist, $r^2 = x^2 + y^2$, $\xi = z/z_R$, $z_R = \pi{\omega_0}^2/\lambda_p$ is the Rayleigh length, $k = 2\pi/\lambda_p$ is the wave vector of the probe beam, and λ_p is the wavelength of the probe beam. Figures 3(a1–e1) are the numerically simulated the hexagonal-coupling field with different spatial configurations according to Eq. (1) with different vertex angles of $\alpha = 30°$, $45°$, $60°$, $90°$, and $120°$, and Figs. 3(a2–e2) are the corresponding output of diffracted probe beam patterns according to Eq. (4). The theoretical parameters are chosen as $\Delta = 5\Gamma_2$ and $\Omega_c = 2\Gamma_2$. Here, the six diffraction sites around the 0th-order diffraction (the middle site) are defined as three pairs of 1st-order diffractions along three directions just like the studies of 1D EIL do [19–21, 23, 24, 27], which integers are labeled in Fig. 3(c2) for a better description.

Figures 3(a3–e3) are the experimentally observed discrete diffraction patterns of the probe beam in photonic graphene with different geometric structures corresponding to the above theoretical hexagonal-coupling field. The experimental results are almost consistent with the numerical simulations graphically. Figure 3(c3) shows a regular photonic graphene when $\alpha = 60°$. The lattice constants are $d_y = d_o \approx 110$ μm in the experiment, where $\theta_y = \theta_o = 0.2°$. In this case, the distribution of 1st-order diffractions of the output probe pattern are highly symmetric and their diffraction intensities are approximately equal. The photonic graphene is stretched along the y direction when $\alpha < 60°$, that is LSPG, and the intensities of 1st-order diffractions in y direction are smaller than those in other two directions, as shown in Figs. 3(a3) and (b3). As α decreases, the lattice constant d_y in y direction becomes gradually higher than d_o in other direction and the stretched degree gradually increases. This causes that the 1st-order diffraction in y direction is far from the 0th-order diffraction and have weaker intensities [24]. The white color region in the centers of the diffraction pattern corresponds to that the intensity of the beam is overexposed, that is, it exceeds the maximum threshold of beam intensity that the CCD can display. On the contrary, the photonic graphene is stretched along the x direction when $\alpha > 60°$, that is TSPG. The diffraction patterns of probe beam and the change of lattice constants show completely opposite performance with that of $\alpha < 60°$, which can be seen in Figs. 3(d3) and (e3). The different geometries of photonic graphene with arbitrarily controllable stretched degrees are realized in our system by varying the vertex angle of the isosceles triangle constructed by three spatial coupling beams arrangement.

According to Eq. (2), the distribution of lattice sites intensity is effectively adjusted by changing two-photon

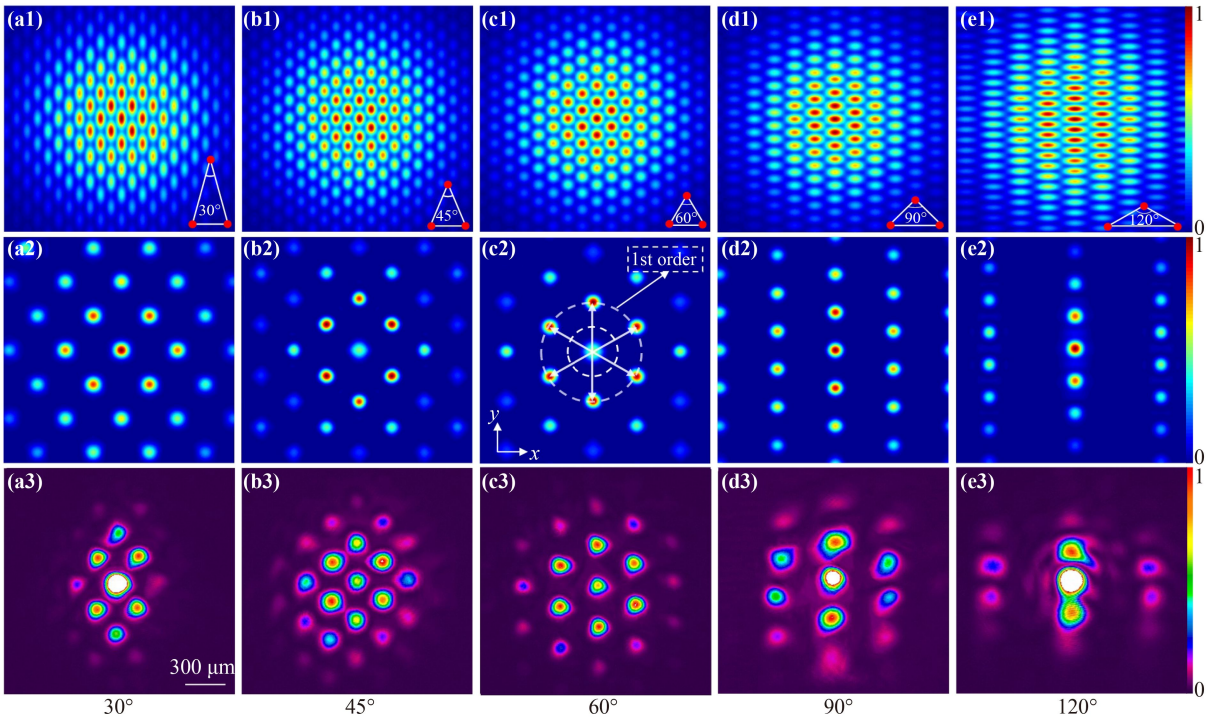

Fig. 3 **(a1–e1)** Theoretically simulated the hexagonal-coupling fields according to Eq. (1) with different vertex angles. (a1) 30°, (b1) 45°, (c1) 60°, (d1) 90°, and (e1) 120°. **(a2–e2)** are the corresponding theoretically simulated diffraction patterns. Here, $\Delta = 5\Gamma_2$, and $\Omega_c = 2\Gamma_2$. **(a3–e3)** show the experimentally observed output diffraction patterns of probe beam. The powers of the coupling and probe beams are 50 mW and 8 mW, respectively, and two-photon detuning is $\Delta = 25$ MHz.

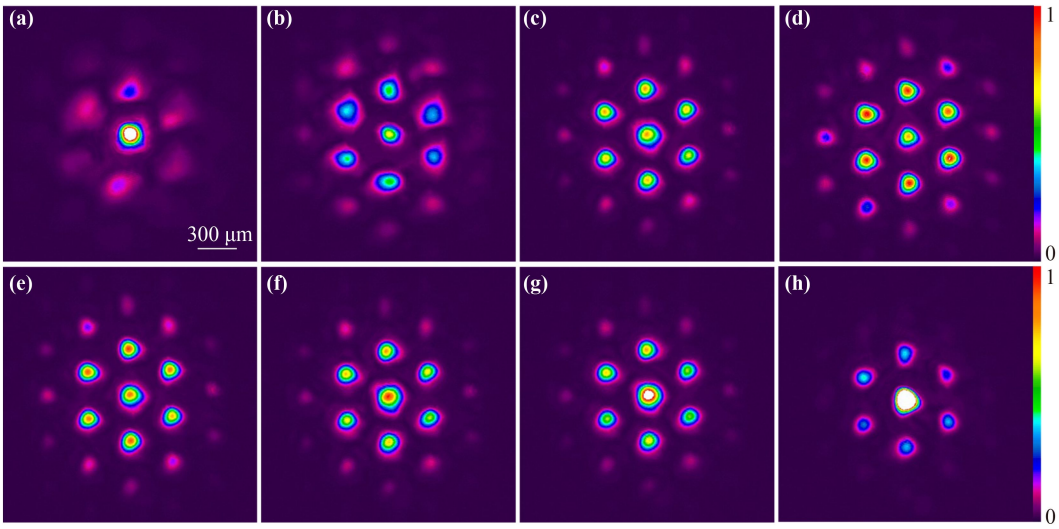

Fig. 4 Diffraction patterns with different two-photon detuning of **(a)** 0 MHz, **(b)** 10 MHz, **(c)** 20 MHz, **(d)** 25 MHz, **(e)** 30 MHz, **(f)** 40 MHz, **(g)** 50 MHz, and **(h)** 60 MHz.

detuning and the coupling beams power. Figure 4 shows the diffraction patterns of a regular photonic graphene with two-photon detunings of $\Delta = 0$, 10, 20, 25, 30, 40, 50, and 60 MHz. The other parameters remain the same as those in Fig. 3(c3). The 1st-order diffraction is indistinctly observed when Δ is relatively low, as shown in Fig. 4(a). The intensities of 1st-order diffractions enhance gradually and higher-order diffractions are clearer with the increase of Δ since the co-interaction of both amplitude and phase modulations to the probe beam [seen in Fig. 4(b)], and the 1st-order intensities are almost the same as that of 0th-order at Δ being 20 MHz [seen in Fig. 4(c)]. Further, the 0th-order intensity is significantly lower than that of 1st-orders with Δ reaches to 25 MHz, and the higher-order diffractions can be clearly observed [seen in Fig. 4(d)]. In this case, the phase modulation dominates owing to far detuned field, which can effectively suppress the nonlinear absorption, enhance the refractivity of the atomic medium and convert from the energy of the 0th-order diffraction into high-order diffractions [24]. The high-order diffractions intensities gradually weakened with continued increasing Δ to exceed 30 MHz, as shown in Figs. 4(f) and (g), mainly because the medium becomes transparent in large Δ and decrease the dispersion to probe beam. Finally, only weak 1st-order diffractions can be observed with two-photon detuning of 60 MHz [seen in Fig. 4(h)]. Different from $\Delta > 0$, the probe beam experiences a self-defocusing process in the atomic medium when $\Delta < 0$, resulting in the indistinct pattern of the far-field diffraction in CCD.

The influence of coupling beams power on diffraction patterns is also investigated experimentally and the results are presented in Fig. 5. Here, the power of coupling beams ranges from 10 to 60 mW in steps of 10 mW. The other parameters are the same as those in Fig. 3(c3). For a weak coupling beams power, only the 1st-order diffraction is observed, and the intensity of the output pattern is mainly concentrated in the 0th-order diffraction, as shown in Figs. 5(a) and (b). The 1st- and even higher-order diffractions become clearer with the growing power of coupling beams, as shown in Figs. 5(c)–(e). The intensity of 0th-order diffraction is lower than that of 1st-orders is clearly observed as the coupling beams power reaches to 50 mW, as shown in Fig. 5(e). Further, the diffraction pattern shows no obvious change compared to that in Fig. 5(e) with a large coupling beams power of 60 mW shown in Fig. 5(f). This is because the enhancement of the EIT efficiency is not apparent for higher coupling beams power. As a result, the lattice sites intensity distribution in photonic graphene changes by adjusting the system parameters.

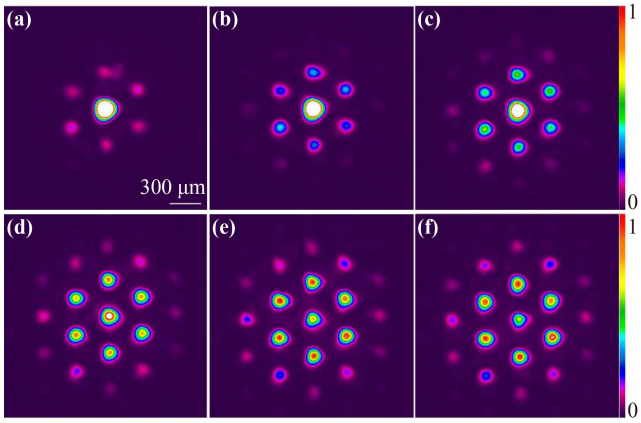

Fig. 5 The diffraction patterns with different coupling beams powers. **(a)** 10 mW, **(b)** 20 mW, **(c)** 30 mW, **(d)** 40 mW, **(e)** 50 mW, and **(f)** 60 mW.

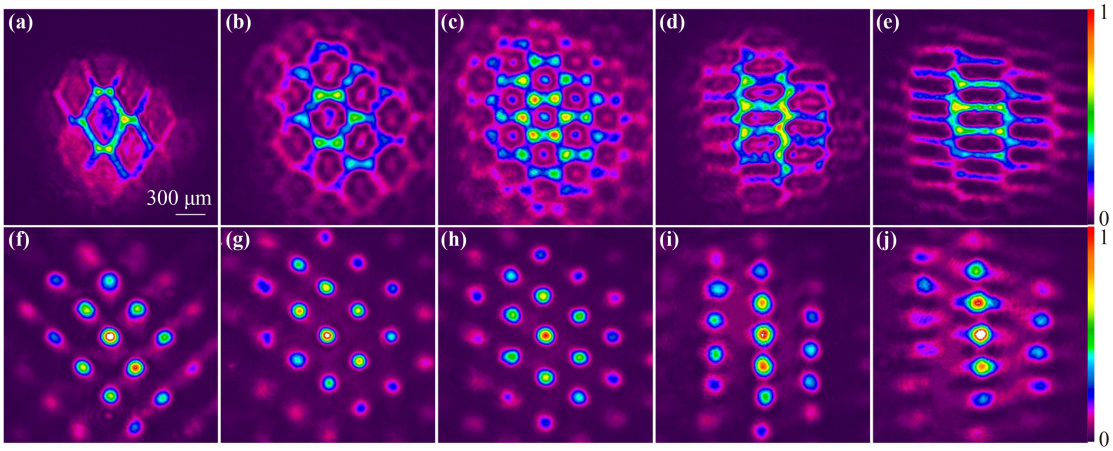

Fig. 6 **(a–e)** The near-field diffraction patterns of the probe beam in photonic graphene with different geometric structures in $\Delta = -15$ MHz. (a) and (b) LSPG, (c) RPG, (d) and (e) TSPG. **(f–j)** are the near-field diffraction patterns corresponding to photonic graphene with geometric structures with $\Delta = 15$ MHz.

Such flexible tunability of photonic graphene in atomic medium is hard to achieve in solid materials, providing an ideal and powerful platform for the further investigation of the novel all-optical devices in the atomic systems.

The near-field diffraction phenomenon of the probe beam in photonic graphene with reconfigurable geometric structures are experimentally observed by placing an imaging lens in front of the CCD with $\Delta = -15$ MHz and $\Delta = 15$ MHz, as shown in Fig. 6. It can be seen that a clear honeycomb profile of the regular photonic graphene is shown in Fig. 6(c) when $\Delta = -15$ MHz. In this case, the refractive index at the honeycomb sites is larger than the hexagonal sites [seen in Fig. 2(e)] [8, 17, 49]. Figures 6(a) and (b) show the near-field diffraction patterns with longitudinally stretched honeycomb profile corresponding to LSPG. On the contrary, the near-field diffraction patterns with honeycomb profile are stretched along the transverse direction, as shown in Figs. 6(d) and (e), that is TSPG. This evolution clearly shows the changes of photonic graphene with reconfigurable geometric structures. Figures 6(f)–(j) exhibit the near-field diffraction phenomenon with a hexagonal intensity distribution when $\Delta = 15$ MHz corresponding to photonic graphene with stretched geometric structures, which are consistent with the far-field diffraction patterns.

4 Conclusions

In summary, photonic graphene with reconfigurable geometric structures is realized theoretically and experimentally by constructing a hexagonal-coupling field in a three-level cascade-type ^{85}Rb atomic medium. The hexagonal field is formed by interference of three identical coupling beams at a small angle θ, propagate along the z-axis to inject into the ^{85}Rb vapor cell to induce photonic graphene. The weak probe beam is diffracted by photonic graphene and exhibits a discrete diffraction pattern with a hexagonal intensity distribution. Different geometries of photonic graphene with stretched structures and the corresponding discrete diffraction patterns are implemented by changing the vertex angle of the isosceles triangle. The dynamic tunability of the lattice sites intensity in photonic graphene is further investigated by changing two-photon detuning and the coupling beams power. This photonic graphene with reconfigurable geometric structures paves the way for further investigation of light transport [42–44] and graphene dynamics [45, 46].

Acknowledgements This work was supported by the National Natural Science Foundation of China (No. 62075121), the Open Fund of MOE Key Laboratory of Weak-Light Nonlinear Photonics (OS 22-2) and Shanxi "1331 Project".

References

1. I. V. Shadrivov, A. A. Sukhorukov, and Y. S. Kivshar, Complete band gaps in one dimensional left-handed periodic structures, *Phys. Rev. Lett.* 95(19), 193903 (2005)
2. T. Baba, Slow light in photonic crystals, *Nat. Photonics* 2(8), 465 (2008)
3. P. Lodahl, A. Floris van Driel, I. S. Nikolaev, A. Irman, K. Overgaag, D. Vanmaekelbergh, and W. L. Vos, Controlling the dynamics of spontaneous emission from quantum dots by photonic crystals, *Nature* 430(7000), 654 (2004)
4. P. Longo, P. Schmitteckert, and K. Busch, Few-photon transport in low-dimensional systems: Interaction-induced radiation trapping, *Phys. Rev. Lett.* 104(2), 023602 (2010)
5. Y. J. Yang, G. Thirunavukkarasu, M. Babiker, and J.

Yuan, Orbital–angular-momentum mode selection by rotationally symmetric superposition of chiral states with application to electron vortex beams, *Phys. Rev. Lett.* 119(9), 094802 (2017)
6. X. D. Wang, H. B. Yu, P. W. Li, Y. Z. Zhang, Y. D. Wen, Y. Qiu, Z. Liu, Y. P. Li, and L. Q. Liu, Femtosecond laser-based processing methods and their applications in optical device manufacturing: A review, *Opt. Laser Technol.* 135, 106687 (2021)
7. T. Ochiai and M. Onoda, Photonic analog of graphene model and its extension: Dirac cone, symmetry, and edge states, *Phys. Rev. B* 80(15), 155103 (2009)
8. Z. Y. Zhang, Y. Feng, S. N. Ning, G. Malpuech, D. D. Solnyshkov, Z. F. Xu, Y. P. Zhang, and M. Xiao, Imaging lattice switching with Talbot effect in reconfigurable non-Hermitian photonic graphene, *Photon. Res.* 10(4), 958 (2022)
9. Y. Plotnik, M. C. Rechtsman, D. H. Song, M. Heinrich, J. M. Zeuner, S. Nolte, Y. Lumer, N. Malkova, J. J. Xu, A. Szameit, Z. G. Chen, and M. Segev, Observation of unconventional edge states in 'photonic graphene', *Nat. Mater.* 13(1), 57 (2014)
10. L. Allen, M. W. Beijersbergen, R. J. C. Spreeuw, and J. P. Woerdman, Orbital angular momentum of light and the transformation of Laguerre–Gaussian laser modes, *Phys. Rev. A* 45(11), 8185 (1992)
11. P. Avouris and F. Xia, Graphene applications in electronics and photonics, *MRS Bull.* 37(12), 1225 (2012)
12. F. S. Deng, Y. Sun, L. J. Dong, Y. H. Liu, and Y. L. Shi, Valley-dependent beam manipulators based on photonic graphene, *J. Appl. Phys.* 121(7), 074501 (2017)
13. K. M. Davis, K. Miura, N. Sugimoto, and K. Hirao, Writing waveguides in glass with a femtosecond laser, *Opt. Lett.* 21(21), 1729 (1996)
14. K. Miura, J. R. Qiu, H. Inouye, T. Mitsuyu, and K. Hirao, Photowritten optical waveguides in various glasses with ultrashort pulse laser, *Appl. Phys. Lett.* 71(23), 3329 (1997)
15. R. R. Gattass and E. Mazur, Femtosecond laser micromachining in transparent materials, *Nat. Photonics* 2(4), 219 (2008)
16. D. Z. Tan, Z. Wang, B. B. Xu, and J. R. Qiu, Photonic circuits written by femtosecond laser in glass: Improved fabrication and recent progress in photonic devices, *Adv. Photonics* 3(2), 024002 (2021)
17. F. Wen, X. Zhang, H. P. Ye, W. Wang, H. X. Wang, Y. P. Zhang, Z. P. Dai, and C. W. Qiu, Efficient and tunable photoinduced honeycomb lattice in an atomic ensemble, *Laser Photonics Rev.* 12(9), 1800050 (2018)
18. S. E. Harris, Electromagnetically induced transparency, *Phys. Today* 50(7), 36 (1997)
19. H. Y. Ling, Y. Q. Li, and M. Xiao, Electromagnetically induced grating: Homogeneously broadened medium, *Phys. Rev. A* 57(2), 1338 (1998)
20. J. P. Yuan, Y. H. Li, S. H. Li, C. Y. Li, L. R. Wang, L. T. Xiao, and S. T. Jia, Experimental study of discrete diffraction behavior in a coherent atomic system, *Laser Phys. Lett.* 14(12), 125206 (2017)
21. J. P. Yuan, C. H. Wu, Y. H. Li, L. R. Wang, Y. Zhang, L. T. Xiao, and S. T. Jia, Controllable electromagnetically induced grating in a cascade-type atomic system, *Front. Phys.* 14(5), 52603 (2019)
22. S. D. Wang, J. P. Yuan, L. R. Wang, L. T. Xiao, and S. T. Jia, Investigation on the Cs $6S_{1/2}$ to 7D electric quadrupole transition via monochromatic two-photon process at 767 nm, *Front. Phys.* 16(1), 12502 (2021)
23. J. P. Yuan, S. C. Dong, C. H. Wu, L. R. Wang, L. T. Xiao, and S. T. Jia, Optically tunable grating in a V + Ξ configuration involving a Rydberg state, *Opt. Express* 28(16), 23820 (2020)
24. H. F. Zhang, J. P. Yuan, S. C. Dong, C. H. Wu, L. R. Wang, L. T. Xiao, and S. T. Jia, All-optical tunable high-order Gaussian beam splitter based on a periodic dielectric atomic structure, *Opt. Express* 29(16), 25439 (2021)
25. J. P. Yuan, C. H. Wu, L. R. Wang, G. Chen, and S. T. Jia, Observation of diffraction pattern in two-dimensional optically induced atomic lattice, *Opt. Lett.* 44(17), 4123 (2019)
26. J. P. Yuan, H. F. Zhang, C. H. Wu, L. R. Wang, L. T. Xiao, and S. T. Jia, Tunable optical vortex array in a two-dimensional electromagnetically induced atomic lattice, *Opt. Lett.* 46(17), 4184 (2021)
27. J. P. Yuan, H. F. Zhang, C. H. Wu, G. Chen, L. R. Wang, L. T. Xiao, and S. T. Jia, Creation and control of vortex beam arrays in atomic vapor, *Laser Photonics Rev.* 2200667, (2023)
28. T. Shui, W. X. Yang, L. Li, and X. Wang, Lop-sided Raman–Nath diffraction in *PT*-antisymmetric atomic lattices, *Opt. Lett.* 44(8), 2089 (2019)
29. Z. Y. Zhang, S. H. Ning, H. Zhong, M. R. Belić, Y. Q. Zhang, Y. Feng, S. Liang, Y. P. Zhang, and M. Xiao, Experimental demonstration of optical Bloch oscillation in electromagnetically induced photonic lattices, *Fundam. Res.* 2(3), 401 (2022)
30. Y. Q. Zhang, D. Zhang, Z. Y. Zhang, C. B. Li, Y. P. Zhang, F. L. Li, M. R. Belić, and M. Xiao, Optical Bloch oscillation and Zener tunneling in an atomic system, *Optica* 4(5), 571 (2017)
31. J. Gao, C. Hang, and G. X. Huang, Linear and nonlinear Bragg diffraction by electromagnetically induced gratings with *PT* symmetry and their active control in a Rydberg atomic gas, *Phys. Rev. A* 105(6), 063511 (2022)
32. J. P. Yuan, S. C. Dong, H. F. Zhang, C. H. Wu, L. R. Wang, L. T. Xiao, and S. T. Jia, Efficient all-optical modulator based on a periodic dielectric atomic lattice, *Opt. Express* 29(2), 2712 (2021)
33. A. W. Brown and M. Xiao, All-optical switching and routing based on an electromagnetically induced absorption grating, *Opt. Lett.* 30(7), 699 (2005)
34. A. Alù and N. Engheta, All optical metamaterial circuit board at the nanoscale, *Phys. Rev. Lett.* 103(14), 143902 (2009)
35. M. C. Rechtsman, J. M. Zeuner, Y. Plotnik, Y. Lumer, D. Podolsky, F. Dreisow, S. Nolte, M. Segev, and A. Szameit, Photonic Floquet topological insulators, *Nature* 496(7444), 196 (2013)
36. Y. Q. Zhang, Z. K. Wu, M. R. Belić, H. B. Zheng, Z. G. Wang, M. Xiao, and Y. P. Zhang, Photonic Floquet topological insulators in atomic ensembles, *Laser Photonics Rev.* 9(3), 331 (2015)

37. Z. Y. Zhang, F. Li, G. Malpuech, Y. Q. Zhang, O. Bleu, S. Koniakhin, C. B. Li, Y. P. Zhang, M. Xiao, and D. D. Solnyshkov, Particle-like behavior of topological defects in linear wave packets in photonic graphene, *Phys. Rev. Lett.* 122(23), 233905 (2019)
38. Z. Y. Zhang, R. Wang, Y. Q. Zhang, Y. V. Kartashov, F. Li, H. Zhong, H. Guan, K. L. Gao, F. L. Li, Y. P. Zhang, and M. Xiao, Observation of edge solitons in photonic graphene, *Nat. Commun.* 11(1), 1902 (2020)
39. Z. Y. Zhang, S. Liang, F. Li, S. H. Ning, Y. M. Li, G. Malpuech, Y. P. Zhang, M. Xiao, and D. Solnyshkov, Spin–orbit coupling in photonic graphene, *Optica* 7(5), 455 (2020)
40. Z. Y. Zhang, Y. Feng, F. Li, S. Koniakhin, C. B. Li, F. Liu, Y. P. Zhang, M. Xiao, G. Malpuech, and D. Solnyshkov, Angular-dependent Klein tunneling in photonic graphene, *Phys. Rev. Lett.* 129(23), 233901 (2022)
41. Q. Tang, B. Q. Ren, V. O. Kompanets, Y. V. Kartashov, Y. D. Li, and Y. Q. Zhang, Valley Hall edge solitons in a photonic graphene, *Opt. Express* 29(24), 39755 (2021)
42. F. S. Deng, Y. M. Li, Y. Sun, X. Wang, Z. W. Guo, Y. L. Shi, H. T. Jiang, K. Chang, and H. Chen, Valley-dependent beams controlled by pseudomagnetic field in distorted photonic graphene, *Opt. Lett.* 40(14), 3380 (2015)
43. F. Lederer, G. I. Stegeman, D. N. Christodoulides, G. Assanto, M. Segev, and Y. Silberberg, Discrete solitons in optics, *Phys. Rep.* 463(1–3), 1 (2008)
44. A. Szameit, I. L. Garanovich, M. Heinrich, A. A. Sukhorukov, F. Dreisow, T. Pertsch, S. Nolte, A. Tünnermann, S. Longhi, and Y. S. Kivshar, Observation of two-dimensional dynamic localization of light, *Phys. Rev. Lett.* 104(22), 223903 (2010)
45. S. E. Skipetrov and P. Wulles, Topological transitions and Anderson localization of light in disordered atomic arrays, *Phys. Rev. A* 105(4), 043514 (2022)
46. D. H. Song, D. Leykam, J. Su, X. Y. Liu, L. Q. Tang, S. Liu, J. L. Zhao, N. K. Efremidis, J. J. Xu, and Z. G. Chen, Valley vortex states and degeneracy lifting via photonic higher-band excitation, *Phys. Rev. Lett.* 122(12), 123903 (2019)
47. D. H. Song, V. Paltoglou, S. Liu, Y. Zhu, D. Gallardo, L. Q. Tang, J. J. Xu, M. Ablowitz, N. K. Efremidis, and Z. G. Chen, Unveiling pseudospin and angular momentum in photonic graphene, *Nat. Commun.* 6(1), 6272 (2015)
48. F. Wen, H. P. Ye, X. Zhang, W. Wang, S. K. Li, H. X. Wang, Y. P. Zhang, and C. W. Qiu, Optically induced atomic lattice with tunable near-field and far-field diffraction patterns, *Photon. Res.* 5(6), 676 (2017)
49. H. F. Zhang, J. P. Yuan, L. T. Xiao, S. T. Jia, and L. R. Wang, Geometric pattern evolution of photonic graphene in coherent atomic medium, *Opt. Express* 31(7), 11335 (2023)
50. F. Pampaloni and J. Enderlein, Gaussian, Hermite-Gaussian, and Laguerre–Gaussian beams: A primer, arXiv: physics/0410021 (2004)